International Journal of Thermophysics, Vol. 27, No. 2, March 2006 (© 2006)
DOI: 10.1007/s10765-006-0050-5

Heat Transport Analysis of Femtosecond Laser Ablation with Full Lagrangian Modified Molecular Dynamics

Y. Yamashita,[1,2] T. Yokomine,[3] S. Ebara,[3] and A. Shimizu[3]

Received January 11, 2005

The purpose of this study is to analyze the heat transport mechanism of femtosecond laser ablation. Under the condition that laser pulse duration is on the order of femtoseconds, a thermal nonequilibrium state between an electron and atom exists and must be taken into account. In order to describe physical phenomena such as heat transport under a nonequilibrium state, a new method, modified molecular dynamics in which molecular dynamics (MD) couples with the two-temperature model (TTM) in a particle-based method, is proposed. In this method, MD simulates the motion of an atom and TTM simulates both electron heat conduction and energy exchange through electron-atom interactions. This approach yields the use of laser intensity as a parameter. For nonequilibrium heat transport, electron heat conduction transports most of the absorbed laser energy and becomes the dominant heat transport mechanism. At thermal equilibrium, above the ablation threshold fluence, electron heat conduction and thermal waves are dominant, while below the ablation threshold fluence, only electron heat conduction is dominant.

KEY WORDS: heat transport mechanism; laser ablation; modified molecular dynamics; two-temperature model.

[1] Department of Advanced Energy Engineering Science, Interdisciplinary Graduate School of Engineering Sciences, Kyushu University, 6-1 Kasugakouen Kasuga, Fukuoka 816-8580, Japan.
[2] To whom correspondence should be addressed. E-mail: yamas@aees.kyushu-u.ac.jp
[3] Division of Energy Engineering Science, Interdisciplinary Graduate School of Engineering Sciences, Kyushu University, 6-1 Kasugakouen Kasuga, Fukuoka 816-8580, Japan.

1. INTRODUCTION

Since its invention, the laser has played an important role in many industrial processes. In recent years, ultra-short pulse lasers have been rapidly developed and employed in material micro-processing. Especially, low fluence femtosecond laser ablation has advantages in precision material processing, that is, there exists neither a liquid phase in the irradiated target nor a corona on the circumference of the ablated hole. On the contrary, for long laser pulses (> 10 ps), a considerable part of the absorbed laser energy rapidly propagates deeply into the target and the liquid phase appears to produce a corona on the circumference of the ablated hole. In precision processing with fs laser ablation, it is difficult to determine the optimal parameters such as laser intensity and pulse duration because physical phenomena, such as heat transport which is the main factor of fs laser ablation, are not well understood.

In order to elucidate the details of heat transport with femtosecond laser irradiation and to determine the optimal parameters, many fundamental studies have been conducted through well-established experiments [1–5] and numerical simulations [6–10]. Experimentally, Momma et al. [3] investigated the dependence of ablation depth on laser pulse energy and pulse duration and demonstrated theoretically and experimentally the existence of optimal parameters, which make precision material processing with fs laser ablation possible. By means of a simple scaling law, they derived the condition to be satisfied by the optimal combination of parameters, e.g., laser intensity and pulse duration. According to that condition, the thermal diffusion length must be shorter than the laser optical penetration depth. The above condition implies that almost all the electron thermal energy is quickly transferred to the lattice through the interaction between electrons and the lattice and the remainder, which is negligibly small, is transferred beyond the optical penetration depth by electron heat conduction.

Furthermore, numerical simulations have been developed through two independent approaches, namely, the two temperature model (TTM) and molecular dynamics (MD). In Ref. 6, Anisimov and Khokhlov proposed a phenomenological TTM to describe the electron and lattice temperatures during short-pulse laser heating of metals. This model, however, is not based on a rigorous derivation. Qiu and Tien [7] succeeded in deriving TTM rigorously from the Boltzmann equation and gave physical meaning to the TTM of Anisimov and Khokhlov. The TTM governing equations consist of electron and lattice energy balance equations. The net energy is exchanged through an electron-lattice interaction term which appears in each equation. The advantage of TTM is the ability to describe the

electron-lattice thermal nonequilibrium state, used to analyze heat transport at ultra-short times. TTM by itself, however, cannot be applied to the deformation of the irradiated target, e.g., the growth of the ablation plume and the formation of the ablation hole. Therefore, in this model, the laser fluence must be limited below the ablation threshold in order to avoid target material ablation.

Conventional MD (CMD) based on electron-lattice thermal equilibrium has been applied to the simulation of laser ablation with picosecond pulse irradiation. However, it cannot be inherently applied to the simulation of fs laser ablation because the electron-lattice thermal nonequilibrium should be taken into account. In addition, CMD cannot correctly simulate electron heat conduction in metals. For almost all metals, CMD underestimates the total thermal conductivity which consists of both electron and lattice thermal conductivities. Concerning fs laser ablation, Herrmann et al. [10] developed a model, in which laser energy is transferred to atomic kinetic energy by means of heat dissipation based on the Debye frequency. By using this method, they investigated the effect of input power and pulse duration on the shape of a laser drilled silicon surface. Atanasov et al. [11] added the effect of ionization to a very similar model and investigated the propagation of a shock wave and the temporal evolution of an ablation plume. Although the above MD simulations are at thermal nonequilibrium, they do not take electron heat conduction into account.

In the present paper, we develop a combined method of MD and TTM, which can describe electron-lattice thermal nonequilibrium and electron heat conduction. In this combined method, TTM is resolved by the so-called particle method, as well as MD. Therefore, we henceforth call our combined method "full Lagrangian modified molecular dynamics" (MMD). By means of MMD, we analyze the behavior of an aluminum thin film irradiated with a femtosecond pulsed laser and compare the results with the ablation threshold fluence of the experiment of Kim et al. [12].

2. FULL LAGRANGIAN MODIFIED MOLECULAR DYNAMICS

For the energy transfer from laser to atom, the following path is assumed. First, laser energy is absorbed by an electron and converted into electron thermal energy, that is, electron temperature. Next, the electron thermal energy dissipates through heat conduction and, at the same time, a part of the thermal energy of the electron transfers into thermal energy of the atom through electron-atom interactions. In this study, MD simulates the motion of the atom, while TTM calculates the heat conduction of

the electronic energy and energy exchange between an electron and atom at thermal nonequilibrium.

2.1. Molecular Dynamics

The MD simulation obeys Newton's second law;

$$m_i \frac{d\mathbf{v}_i}{dt} = -\nabla E_i \tag{1}$$

$$\frac{d\mathbf{r}_i}{dt} = \mathbf{v}_i \tag{2}$$

where subscript i refers to atom i, $\mathbf{v}$ is the velocity vector of the atom, $\mathbf{r}$ is the position vector of the atom, t is time, m is the mass of the atom, and E is the inter-atomic potential.

For the inter-atomic potential appearing in Eq. (1), the embedded atom method (EAM) potential [13] is adopted as it describes metal transients well. The EAM consists of a pair potential part and a many-body interaction part as follows:

$$E_i = F_{EAM_i}(\rho_i) + \frac{1}{2}\sum_{\substack{j \\ i \neq j}}^{N} \phi(r_{ij}) \tag{3}$$

where ρ_i is the electron density at the position of atom i, r_{ij} is the distance between atoms i and j, F_{EAM} is the embedded energy, $\phi(r_{ij})$ is the pair potential energy at distance r_{ij}, and N is the total number of atoms. In Eq. (3), F_{EAM}, ρ_i, and $\phi(r_{ij})$ are calculated from the following equations:

$$\begin{aligned} F_{EAM_i}(\rho_i) = & -E_c\left[1 - \frac{\alpha}{\beta}\ln(\rho_i)\right]\rho_i^{\frac{\alpha}{\beta}} \\ & + \frac{1}{2}\phi_0 \sum_{m=1}^{3} s_m \exp\left[-\left(\sqrt{m}-1\right)\gamma\right] \\ & \times \left[1 + \left(\sqrt{m}-1\right)\delta - \sqrt{m}\frac{\delta}{\beta}\ln(\rho_i)\right]\rho_i^{\frac{\sqrt{m}\gamma}{\beta}} \end{aligned} \tag{4}$$

$$\rho_i(r_{ij}) = \sum_{j \neq i}^{N}\sum_{l=0}^{5} \frac{c_l}{12}\left(\frac{r_0}{r_{ij}}\right)^l \tag{5}$$

$$\phi(r_{ij}) = -\phi_0\left[1 + \delta\left(\frac{r_{ij}}{r_0} - 1\right)\right]\exp\left[-\gamma\left(\frac{r_{ij}}{r_0} - 1\right)\right] \tag{6}$$

Table I. Potential Parameters

Constatnts	Value	Constants	Value
E_c	3.39 eV	c_1	−6.83764
ϕ_0	0.1318 eV	c_2	26.75616
r_0	0.28638 nm	c_3	−47.16495
α	4.60	c_4	36.18925
β	7.10	c_5	−8.60834
γ	7.34759	s_1	12
δ	7.35	s_2	6
c_0	0.64085	s_3	24

where E_c is the collective energy, r_0 is the distance of nearest atoms, and α, β, γ, δ, c_l, s_m, and ϕ_0 are potential parameters. In this model, the cutoff distance of $\rho_i(r_{ij})$ and $\phi(r_{ij})$ lies between the third and fourth neighbors of the fcc crystal. These constants are shown in Table I. Furthermore, the following cutoff function has been introduced to make the potential function go to zero smoothly between r_n and r_c. The form can be written as

$$q(r) = \begin{cases} 1 & (r \le r_n) \\ (1-x)^3\left(1+3x+6x^2\right) & (r_n \le r \le r_c) \\ 0 & r \ge r_c \end{cases} \tag{7}$$

$$x = \frac{r - r_n}{r_c - r_n} \tag{8}$$

where $r_n = 1.75r_0$, and r_c is a cutoff distance equal to $1.95r_0$

The modified Verlet method is used for time integration of Eqs. (1) and (2).

2.2. Two-Temperature Model

TTM consists of two governing equations [7] that are energy balances of an electron and atom as follows:

$$C_e(T_e)\frac{DT_e}{Dt} = \nabla\left(K_e \nabla T_e\right) - G\left(T_e - T_l\right) + S(\mathbf{r}, t) \tag{9}$$

$$C_l \frac{DT_l}{Dt} = G(T_e - T_l) \tag{10}$$

where subscripts e and l denote an electron and atom, respectively. D/Dt is the total derivative, C is the heat capacity per unit volume, T is the temperature, K is the thermal conductivity, S is the absorbed laser energy, and G is the electron-atom interaction coefficient. On the right-hand side of Eq. (9), the first term expresses electron energy dissipation via heat conduction described by Fourier's law that assumes heat propagation at infinite speed. The second term is the energy exchange between an atom and electron. The third term is the source term originating in the absorbed laser energy at each electronic position $\mathbf{r}$ and time t. The details of the laser absorption model are explained in the next section. In our method, Eqs. (9) and (10) are calculated three-dimensionally in Lagrangian form by means of the material point semi-implicit (MPS) method [14].

The heat capacity and thermal conductivity depend on temperature and are defined by Qiu and Tien [7] as follows:

$$C_e(T_e) = \gamma T_e \tag{11}$$

$$K_e = k_e \frac{T_e}{T_l} \tag{12}$$

Values for the constants for Al at 300 K in Eqs. (9) and (10) are $\gamma = 91\,\mathrm{J \cdot m^{-3} \cdot K^{-2}}$, $C_l = 2.41 \times 10^6\ \mathrm{J \cdot\ m^{-3} \cdot K^{-1}}$, $k_e = 2.36 \times 10^2 \mathrm{W \cdot\ m^{-1} \cdot K^{-1}}$, and $G = 7.05 \times 10^{16} \mathrm{W \cdot\ m^{-3} \cdot K^{-1}}$.

In order to couple MD with TTM, the atomic temperature T_l in TTM at the position obtained by MD is defined by the kinetic energy of an atom;

$$T_l = \frac{1}{3k_B} m_i \mathbf{v}_i \cdot \mathbf{v}_i \tag{13}$$

where k_B is the Boltzmann constant. On the other hand, the electron temperature is also defined at the position of MD atom "i". In Eq. (9), the diffusion term is calculated using the MPS method;

$$\nabla \cdot (K_e \nabla T_{ei}) = A \sum_{j \neq i} \left[k_e \frac{T_{ej} + T_{ei}}{T_{lj} + T_{li}} \cdot \frac{2}{n_i + n_j} \left(T_{ej} - T_{ei} \right) W\left(r_{ij} \right) \right] \tag{14}$$

where A is a constant, $W(r_{ij})$ is the weight function, and n is the particle number density. Constant A, the weighting function, and the particle number density are defined as follows:

$$A = \frac{2d \int_V W(r) r^2 dv}{\int_V W(r)\, dv} \tag{15}$$

$$W(r_{ij}) = \begin{cases} \frac{r_c}{r_{ij}} - 1 & r_{ij} \le r \\ 0 & r_c \le r_{ij} \end{cases} \tag{16}$$

$$n_i = \sum_j W\left(r_{ij}\right) \tag{17}$$

where d is the space dimension, dv is an infinitesimal volume, and V is the volume of a sphere with radius r_c, and r is variable from 0 to r_c.

The resulting change of atomic temperature by TTM feeds back to the kinetic energy of the same atom in MD by means of scaling each component of velocity as follows:

$$\mathbf{v}^{new} = \mathbf{v}^{old}\left[\frac{E_{exc}}{E_{kin}} + 1\right]^{\frac{1}{2}} \tag{18}$$

$$E_{exc} = \frac{3}{2}k_B(T_l^{new} - T_l^{old}) \tag{19}$$

where E_{kin} denotes the kinetic energy of the atom before the TTM calculation and E_{exc} denotes the energy transferred from an electron to an atom through electron-atom interactions after the TTM calculation. Superscripts "old" and "new" represent the values before and after TTM calculations, respectively.

2.3. Laser Model

For the source term appearing in Eq. (9), the spatial distribution of the absorbed laser energy obeys the Lambert-Beer law and is calculated by means of tracing the energy carrier [15]. In this model, the energy carrier has no mass and size, only energy and is assumed to move much faster than atoms and electrons so that, during tracing, the energy carrier, atoms, and electrons are stationary. The energy carrier is a virtual particle in the simulation and differs completely from a photon. Each energy carrier has the same amount of energy. The trajectories of the energy carriers are determined by means of Monte Carlo calculations. A total of 60,000 energy-carrier particles are initially distributed from the laser irradiated surface to the bottom of the system in the following scheme. Depthwise, they are distributed exponentially, while the transverse distribution is assumed uniform;

$$\mathbf{r} = (R_x L_x, R_y L_y, Z_{high} - s) \tag{20}$$

$$s = -\lambda \log(1 - R_s) \tag{21}$$

where R_s, R_x, and R_y are random numbers, L_x and L_y are sizes of the system in the x- and y-directions, respectively, Z_{high} is the position of an atom staying at the highest position of the model system, and λ is the skin depth.

The velocity distribution of the initial motion of the energy carrier is isotropic. It is assumed that the energy carrier gives 70% of its energy to electron thermal energy and scatters isotropically when it collides with electrons. This value of 70% is determined empirically so as to result in reproducing the Lambert-Beer law. When either the energy of the energy carrier is lower than 0.1% of the initial value due to absorption, the tracing to the carrier is complete. The scattering direction, c_p, is determined by using two uniform random numbers, R_η and R_θ, and two angles, η and θ, where η and θ are the directional angles of the scattered energy carrier with respect to the z- and x-axes, respectively, in the x-y plane. The relationships among these variables are as follows [15]:

$$\eta = \cos^{-1}\left(1 - 2R_\eta\right) \tag{22}$$

$$\theta = 2\pi R_\theta \tag{23}$$

Therefore, the direction of the energy carrier after scattering by an electron can be written as

$$c_p = (\cos\theta \sin\eta, \sin\theta \sin\eta, \cos\eta) \tag{24}$$

2.4. Model System and Parameters

The model system is shown in Fig. 1. Aluminum is chosen as the target material. The initial system is an fcc crystal composed of 80,000 atoms with dimensions $4.04 \times 4.04 \times 80.9\,\text{nm}^3$. A normal periodic boundary condition, which is widely used in molecular dynamics, is imposed on the x-z and y-z planes; a mirror image boundary is applied at the bottom; and an open boundary is used at the top of the system. Once the atom leaves the top of the system, the tracing calculation ceases. Five atomic layers from the bottom are kept at 300 K serving as a heat sink. As the initial condition, the whole system is set at 300 K. Calculation parameters are shown in Table II. Ionization and plasma are not considered here because the laser energy is low. The pulse duration is fixed at 100 fs, and the laser intensity is varied in the range from 1.0×10^{12} to 5.0×10^{12} $\text{W} \cdot \text{cm}^{-2}$. In this study, the laser wavelength is assumed to be 1064 nm so that the absorption coefficient is about $2 \times 10^7 \text{m}^{-1}$ [16]. The skin depth is set to a

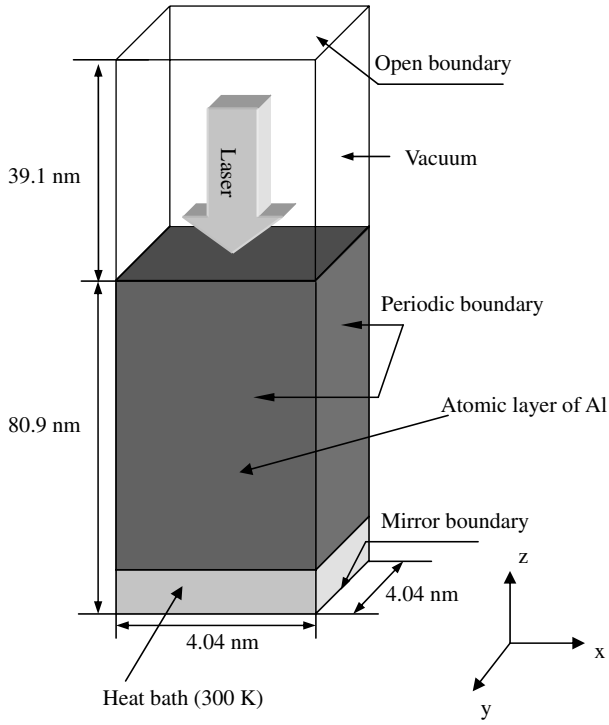

Fig. 1. Schematic of calculation system of Modified Molecular Dynamics simulation.

Table II. Calculation Parameters

	Laser intensity ($W \cdot cm^{-2}$)	Pulse duration (fs)	Fluence ($J \cdot cm^{-2}$)	Time step of MD (fs)	Time step of TTM (as)
Case-A	1.0×10^{12}	100	0.1	0.1	1.0
Case-B	2.5×10^{12}	100	0.25	0.1	1.0
Case-C	5.0×10^{12}	100	0.5	0.1	1.0

value of 5 nm. The time step of TTM is determined as satisfying a numerical stable condition.

2.5. Physical Quantities

In order to calculate statistical quantities, the system is divided into 160 control volumes of 0.75 nm thickness in the direction of the depth.

The averaged atom temperature is defined in each control volume as follows:

$$T = \frac{1}{3Nk_B} \sum_{i}^{N} m_i \mathbf{v}_i \cdot \mathbf{v}_i \tag{25}$$

The pressure is obtained from the normal stresses defined in Cartesian coordinates;

$$P = \frac{1}{3} \left(\sigma_{xx} + \sigma_{yy} + \sigma_{zz} \right) \tag{26}$$

$$V\sigma_{\alpha\beta} = \frac{\partial}{\partial t} \left(\sum_{i}^{N} m_i r_{i\alpha} v_{i\beta} \right) = \sum_{i}^{N} \left(m_i \dot{r}_{i\alpha} v_{i\beta} + m_i r_{i\alpha} \dot{v}_{i\beta} \right) \tag{27}$$

where $\sigma_{\alpha\beta}$ denotes the stress tensor, V is the control volume, dotted quantities indicate time derivatives, and subscripts α and β refer to axes in Cartesian coordinates.

3. RESULTS AND DISCUSSION

3.1. Heat Transport Mechanism

Figure 2 shows the relaxation time for an electron and atom to reach thermal equilibrium. We define the condition that the electronic temperature is nearly equal to the atomic temperature at electron-atom thermal equilibrium. In Fig. 2, the vertical axis shows the average particle ensemble temperature. In the legend, Case-A, -B, and -C correspond to the parameters given in Table II. Laser irradiation is terminated at 0.1 ps; therefore, the electronic temperature at 0.1 ps is highest over the whole time scale. After 0.1 ps, for all cases, the electronic temperature gradually decreases because the electronic thermal energy is converted into atomic thermal energy through electron-atom interactions. The relaxation times for Case-A, -B, and -C are 4, 5, and 7 ps, respectively. Therefore, it is concluded that the relaxation time scale is regarded to be several ps and the relaxation time depends on laser fluence.

Transient electron temperature profiles are shown in Fig. 3. In the legend of Fig. 3, Case-A, -B, and -C correspond to the parameters given in Table II, the same as in Fig. 2. It is found that the electronic temperature level depends on laser fluence. The temperature level of Case-C becomes highest in all cases. Except for the dependence of the temperature level on laser fluence, the behavior of temperature profiles does not differ from

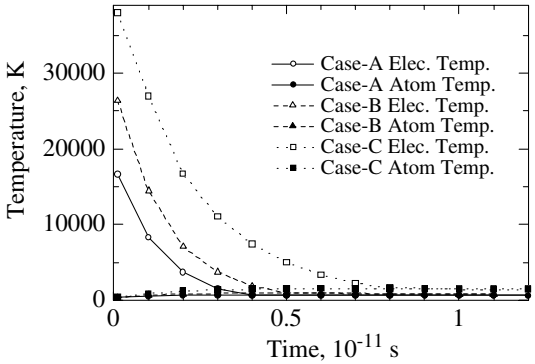

Fig. 2. Time evolution of averaged temperature profiles for both electron and atom.

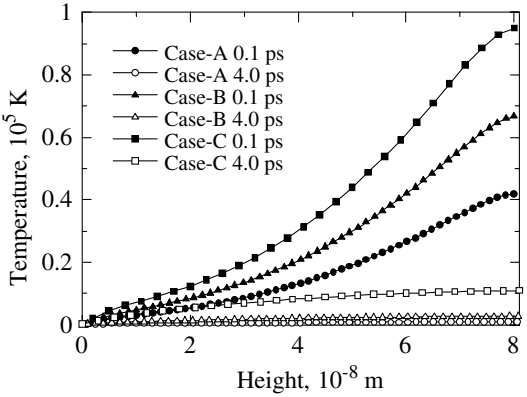

Fig. 3. Spatial distributions of electron temperature at $t = 0.1$ and 4.0 ps for all cases.

each other. For all cases, the laser energy has already been distributed from surface to bottom by electronic heat conduction at 0.1 ps. From the point of view of conventional thermal diffusion, the heat diffusion speed of these results is extremely fast. Although conventional theory is based on electron-atom thermal equilibrium, this simulation is based on electron-atom thermal nonequilibrium. In thermal nonequilibrium, the electronic temperature is much higher than the atomic one. Therefore, the electronic temperature system has a large temperature gradient that cannot be considered in conventional thermal diffusion. This large temperature gradient leads to ultra-fast heat conduction in the electronic system.

For heat transport mechanisms during thermal nonequilibrium, it is concluded that electron heat conduction is dominant regardless of laser fluence. After reaching thermal equilibrium, the main heat transport mechanism is shifted from electrons to both atoms and electrons. Figures 4, 5, and 6 show the transient temperature profiles of Case-A, -B, and -C, respectively. These cases correspond to the parameters given in Table II. In Fig. 4, after 0.1 ps, the atomic temperature continues to increase until 4.0 ps through electron-atom interactions. According to Fig. 2, the electronic and atomic temperatures reach thermal equilibrium at 4.0 ps. Therefore, the atomic temperature level does not increase after 4.0 ps. For Fig. 5, the behavior of the atomic temperature profile shows a similar trend to that in Fig. 4. In Figs. 4 and 5, the temperature profiles of Case-A and -B do not have a reverse temperature gradient. Therefore, their heat transport type is diffusion in which the main energy transport mechanism is heat conduction. For the temperature profile of Case-C in Fig. 6, a reverse temperature gradient appears. The maximum value appears at 55 nm in the z-direction at 4 ps and at 28 nm in the z-direction at 8 ps. The minimum value appears at 61 nm in the z-direction at 4 ps and at 42 nm in the z-direction at 8 ps. The appearance of a peak value corresponds to the propagation of the pressure.

Figure 7 shows the velocity component in the z-direction for Case-C. The front of the pressure wave corresponds to the position where the temperature gradient changes from positive to negative. The position of the pressure wave, therefore, almost corresponds to the position of the peak temperature value. Therefore, it is concluded that, near the front region of the pressure wave, the target is compressed locally and the temperature

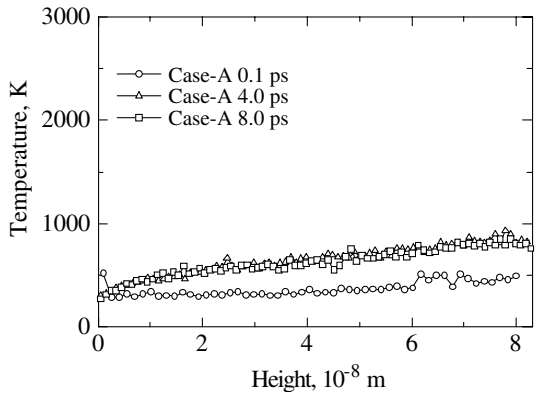

Fig. 4. Spatial distributions of atom temperature at $t = 0.1$, 4.0 and 8.0 ps for Case-A.

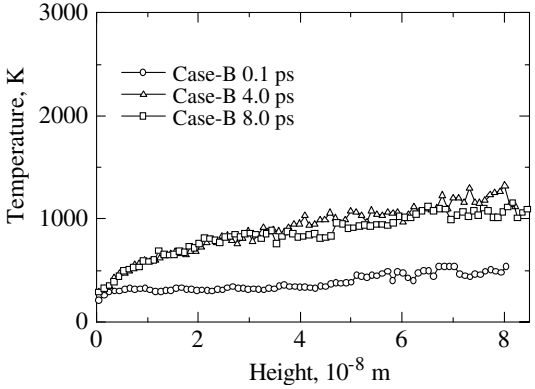

Fig. 5. Spatial distributions of atom temperature at $t = 0.1$, 4.0 and 8.0 ps for Case-B.

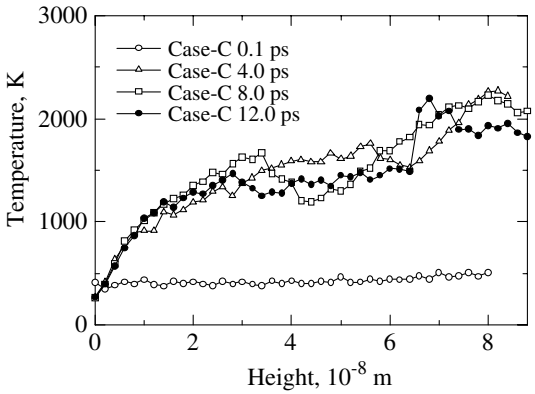

Fig. 6. Spatial distributions of atom temperature at $t = 0.1$, 4.0, 8.0 and 12.0 ps for Case-C.

rises, while, at the rear end, the target expands locally and the temperature decreases. In addition, the pressure waves transport large kinetic energy that can be converted into thermal energy via some friction mechanisms. In other words, the pressure wave transports thermal energy in the form of kinetic energy. Here, we call the pressure wave that can lead to a drastically large temperature change a "thermal wave." Furthermore, the heat transport mechanism for which thermal waves transport thermal energy is defined as "wave-type heat transport mechanism." Since electron heat conduction dissipates thermal energy during a traveling thermal wave, for a wave-type heat transport mechanism, the major energy transport mechanism is concluded to be both electron heat conduction and thermal waves.

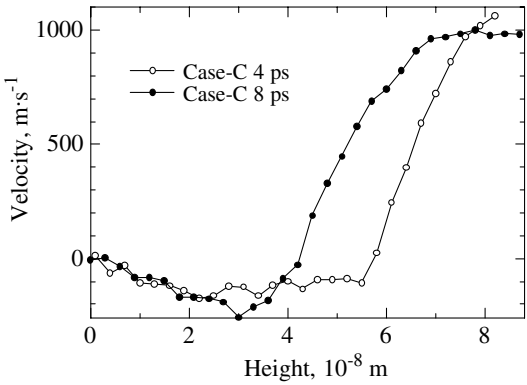

Fig. 7. Spatial distributions of velocity component in z-direction at $t = 4.0$ and 8.0 ps for Case-C.

Considering the target behavior due to phase change in each case appearing in Table II, the phenomenological mechanism of the appearance of wave-type heat transport could be clear. Figures 8 and 9 show the target expansion in Cases A and B, respectively. Figure 10 shows the time evolution of the target expansion including the ablation plume in Case C. For Case A, phase change does not occur. On the other hand, for Cases B and C, it is confirmed that the phase changes because the lattice structure disappears around the surface. In Case B, phase changes from solid to liquid occur, while, in Case C, phase changes from solid to gas occur. In Case C, during phase change from solid to liquid, the volume expands violently due to phase change during an ultra-short time. The observed volume expansion in Case B during the ultra-short time is calm compared with that of Case C. The difference between both behaviors of phase change is considered as the phenomenological threshold for appearance of wave-type heat transfer. The propagation velocity of the thermal wave is nearly equal to the velocity of the elastic wave ($6420\,\mathrm{m \cdot s^{-1}}$). This result supports the analysis [17] of Ohmura et al.

3.2. Ablation Threshold Fluence

In this section, phenomenological considerations are based on an analysis of Figs. 8 to 10. In Case A, the phase does not change so that the lattice structure still remains. In Case B, phase change from solid to liquid occurs over 82 nm and between 75 and 80 nm at 8 ps. However, the rest still remains a lattice structure. Hereafter, we call this structure a "sandwich structure." The time evolution of such a sandwich structure can be explained as follows. Most of the thermal energy is transported by

electron heat conduction before an atom absorbs enough thermal energy to undergo phase change through electron-atom interactions. Afterwards, the electron temperature profile becomes almost flat due to electron heat conduction in the upper part of the system, and the end atomic temperature begins to increase with the temperature gradient. Vacancies and impurities are not included in the calculations for the system.

In this picture, it can be assumed that atoms remain in their lattice sites under superheating conditions. The lattice structure must be broken one by one at locations where atoms are thermally perturbed. At the origin of perturbation the velocity gradient in the z direction and the behavior of atoms at the interface between the target and vacuum can be considered. Figure 11 shows temperature and velocity components in the z direction for Case B. At 2 ps, the atomic temperature is beyond melting (933 K) in the upper part of the system. Then, the velocity component in the z direction exhibits a sharp gradient from 65 to 75 nm in height and almost a flat profile above 75 nm. Hereafter, "Part A region" denotes from 65 to 75 nm in height and "Part B" denotes above 75 nm height. This sharp gradient leads to irregular expansion in the Part B region. Irregular expansion becomes the system perturbation and leads to phase change. In the Part A region, the relative position among atoms does not change because of the constant velocity in the z direction. Therefore, only at the interface between the target and vacuum is the lattice perturbed and phase change occurs near the target surface. Regions undergoing no such interface effects retain the lattice structure. This is the reason why the sandwich structure has already been formed at 2 ps. Parts A and B regions at 2 ps propagate at about $450\,\mathrm{m \cdot s^{-1}}$ and break the lattice structure.

As time lapses, the progression of phase change and its sandwich structure appears gradually. In Case C, the lattice structure is completely broken and the solid target changes into fluid because the laser fluence is high enough to generate ablation. At 67 nm in the system, it is confirmed that one large void continues to grow after 12 ps. The plume temperature is always about 2000 K. Here, the plume is defined as the atom cluster existing above the void. On the other hand, the temperature of the remaining lattice never exceeds 2000 K. Although it is unknown whether the value of 2000 K has meaning or not, it seems that the position of void generation is at the interface between the high- and low-temperature regions. The details of the void generation mechanism are still open to discussion.

3.3. Ablation Threshold Fluence

The value of ablation threshold fluence strongly depends on the ability to model the heat transport mechanism during the ultra-short time.

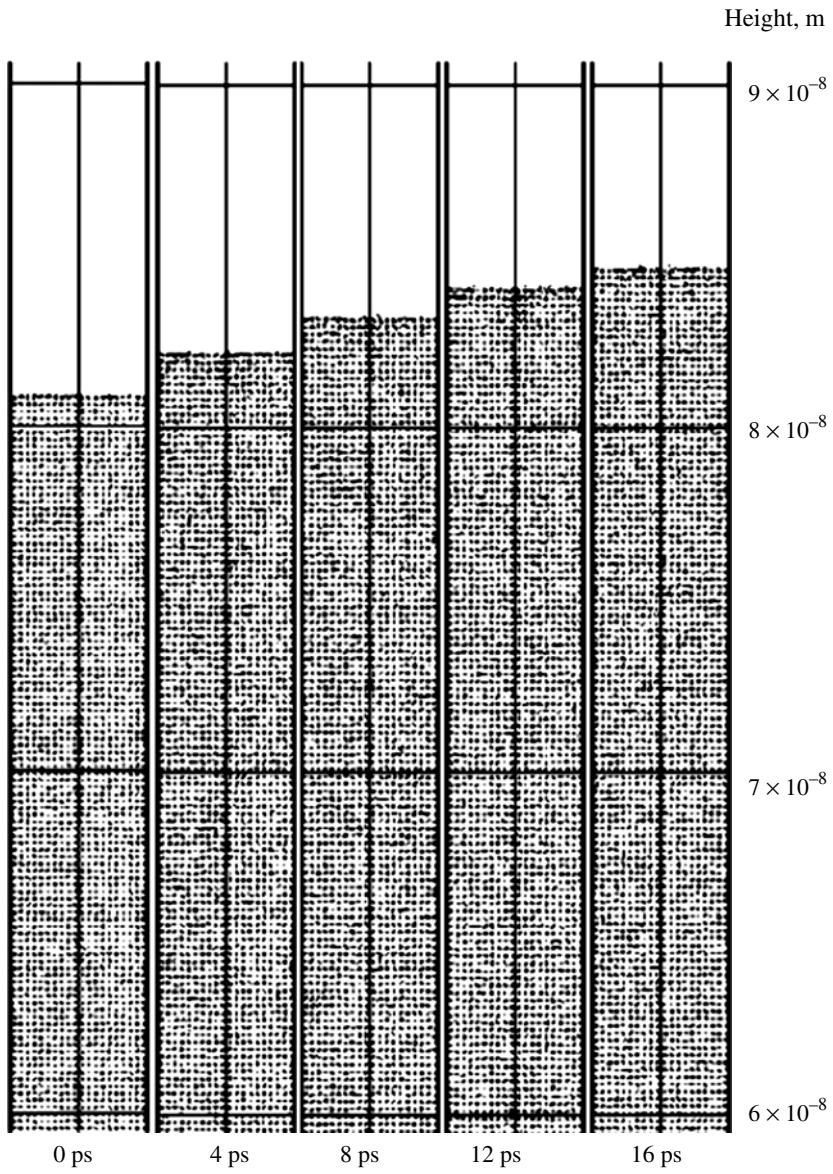

Fig. 8. A series of snapshots of atoms locating near surface for Case-A.

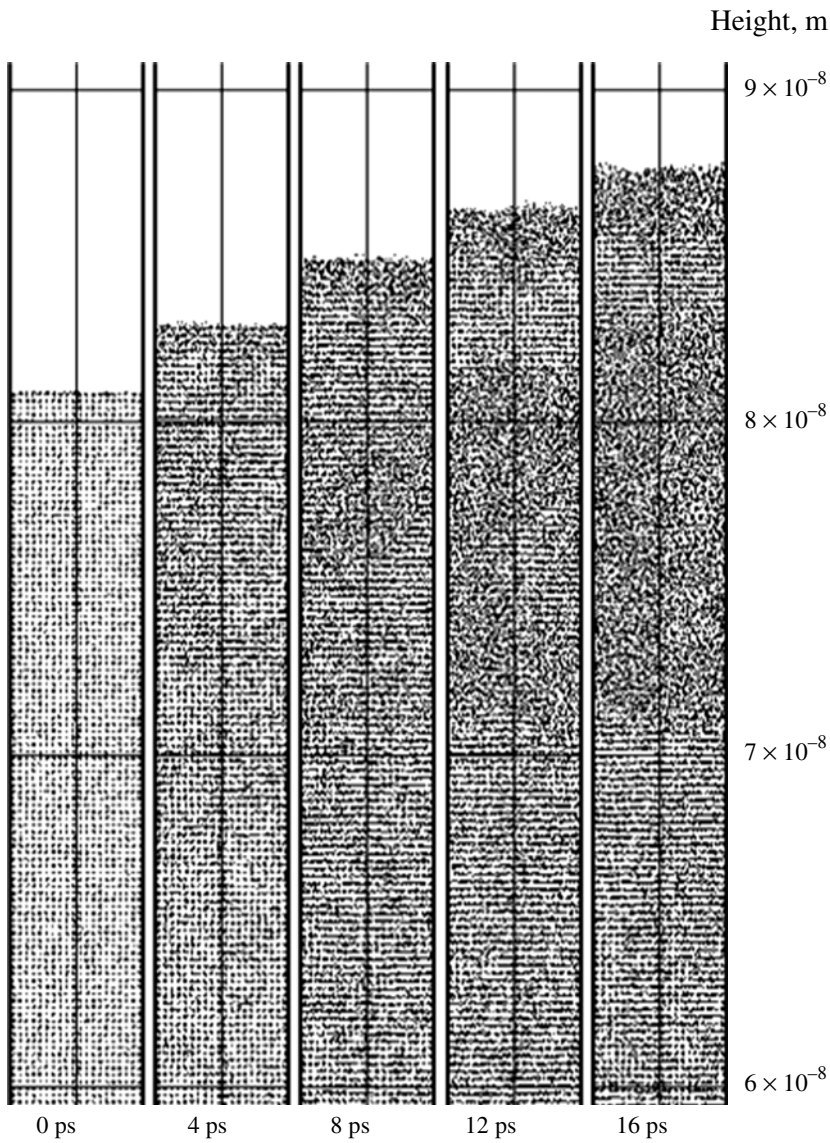

Fig. 9. A series of snapshots of atoms locating near surface for Case-B.

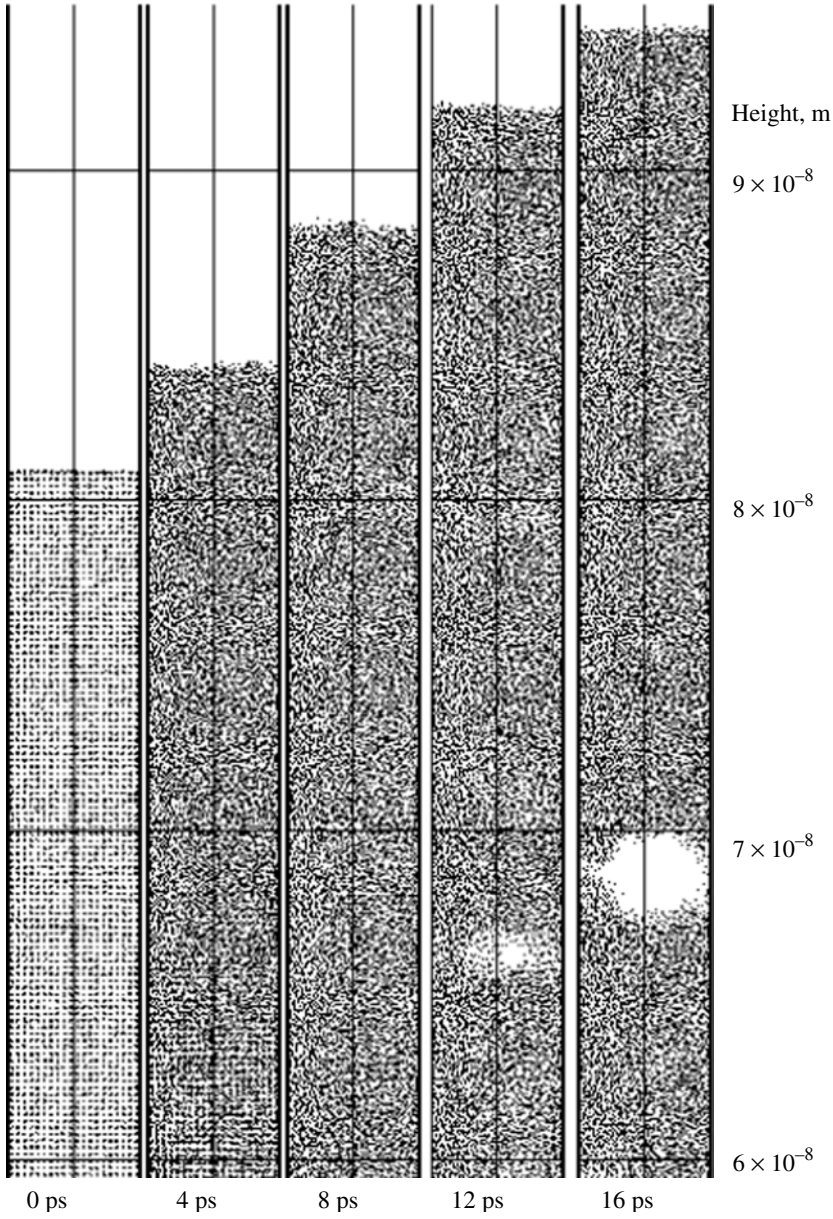

Fig. 10. A series of snapshots of atoms locating near surface for Case-C.

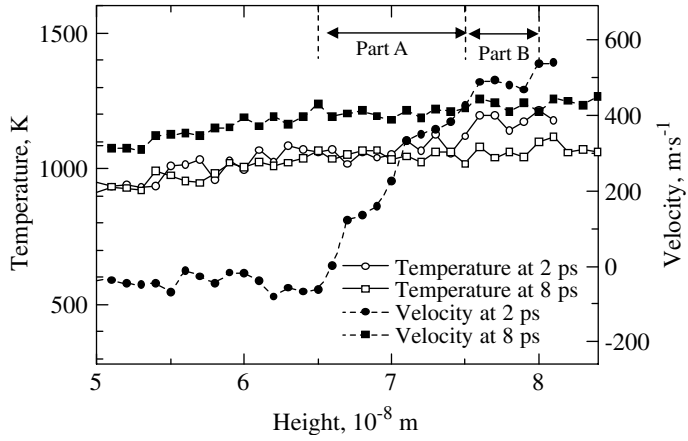

Fig. 11. Spatial profiles of temperature and velocity component in z direction at $t = 2.0$ and 8.0 ps for Case-B.

Therefore, it is desirable to verify the validity of numerical methods. Ablation occurs when the temperature of the irradiated surface reaches the boiling point (2740 K), or the target is divided and voids appear in some regions. The former is monitored from the atomic temperature profile, while the latter is visually monitored from the existence of voids or the scattering behavior of atoms. Concerning the present calculation results, the surface temperature is less than the boiling point temperature for all cases. However, in Case C, a large void exists in the middle of the system; therefore, the ablation threshold fluence is considered to be about $500\,\mathrm{mJ \cdot cm^{-2}}$. Referring to the experiment of Kim et al. [12], the ablation threshold fluence of aluminum irradiated with a fs pulsed laser is $105\,\mathrm{mJ \cdot cm^{-2}}$. Indeed, the calculated threshold fluence is five times as high as the experimental value, but the deviation from the experimented value is not too much. The model system has a low temperature heat sink at the bottom, which consumes the extra laser energy needed to ablate the target. That is, it leads to an overestimation of the ablation threshold fluence. In order to avoid this problem, it is necessary to expand the calculation domain sufficiently, which adds an extremely high calculation cost. An efficient scheme for extending the calculation domain without over-extending the computer cost is required and is currently under investigation. Now, our team is developing a new method in order to fix this problem without adding numerous calculation costs.

4. CONCLUSIONS

The heat transport mechanism and the behavior of a surface expansion/ablation plume with irradiation by a femtosecond laser have been studied by using MMD. Some important results are obtained. First, MMD reproduces well the ablation fluence of fs laser ablation. Second, the relaxation time of the electron-atom thermal nonequilibrium depends on the laser fluence and its duration is several ps. Third, at electronic and atomic thermal nonequilibrium, free electrons mainly transport thermal energy regardless of laser fluence. After reaching thermal equilibrium, the dominant heat transport mechanism in the target irradiated with low fluence and ultra-short pulse laser is electronic heat conduction. On the other hand, with high fluence, electron heat conduction and thermal waves are dominant during thermal equilibrium between electrons and atoms. Furthermore, the atomic temperature profile shows a wave-type heat transport mechanism. In future work, we will take the effects of the non-Fourier's nature of electron heat conduction into account in order to simulate heat transport of fs laser ablation more accurately.

REFERENCES

1. W. S. Fann, R. Storz, H. W. K. Tom, and J. Bokor, *Phys. Rev. Lett*. **68**:2834 (1992).
2. T. Q. Qiu and C. L. Tien, *Int. Heat Mass Transfer* **37**:2799 (1994).
3. C. Momma, B. N. Chichkov, S. Nolte, F. Alvensleben, A. Tuennermann, H. Welling, and B. Wellegehausen, *Optics Comm.* **129**:134 (1996).
4. S. Nolte, C. Momma, H. Jacobs, A. Tuennermann, B. N. Chichkov, B. Wellegehausen, and H. Welling, *J. Opt. Soc. Am. B* **14**:2716 (1997).
5. S.-S. Wellershoff, J. Hohlfeld, J. Guedde, and E. Matthias, *Appl. Phys. A* **69**:99 (1999).
6. S. I. Anisimov and V. A. Khokhlov, *Instabilities in Laser-Matter Interaction* (CRC Press, Boca Raton, Florida, 1995).
7. T. Q. Qiu and C. L. Tien, *J. Heat Transfer* **115**:835 (1993).
8. T. Q. Qiu and C. L. Tien, *Int. J. Heat Mass Transfer* **35**:719 (1992).
9. R. F. W. Herrmann, J. Gerlach, and E. E. B. Campbell, *Nucl. Instrum. Methods Phys. Res., Sect. B* **122**:401 (1997).
10. R. F. W. Herrmann, J. Gerlach, and E. E. B. Campbell, *Appl. Phys. A* **66**:35 (1998).
11. P. A. Atanasov, N. N. Nedialkov, S. E. Imamova, A. Ruf, H. Huegel, F. Dausinger, and P. Berger, *J. Appl. Surf. Sci.* **186**:369 (2002)
12. M. K. Kim, T. Takao, Y. Oki, and M. Maeda, *Jpn. J. Appl. Phys.* **39**:6277 (2000).
13. J. Mei and J. W. Davenport, *Phys. Rev. B* **46**:21 (1992).
14. S. Koshizuka, H. Tamako, and Y. Oka, *Comput. Fluid Dynamics* **4**:29 (1995).
15. K. Ezato, *Study of Numerical Analysis Method for Heat and Particle Transport in High Energy Density Machines* (Ph. D. Thesis, Kyushu University, Fukuoka, Japan, 1997).
16. E. Ohmura, I. Fukumoto, and I. Miyamoto, *Proc. SPIE* **4088**:84 (2000).